PAPER • OPEN ACCESS

Measurements and modeling of type-I and type-II ELMs heat flux to the DIII-D divertor

To cite this article: R. Perillo *et al* 2023 *Nucl. Fusion* **63** 086031

View the article online for updates and enhancements.

Measurements and modeling of type-I and type-II ELMs heat flux to the DIII-D divertor

R. Perillo[1],* , J.A. Boedo[1], C.J. Lasnier[2] , R.A. Pitts[3] , M. Brank[4], I. Bykov[5], J.D. Coburn[6] , F. Glass[5], C. Marini[1] , T. Osborne[5], M. Riding[7], D.L. Rudakov[1] , J.G. Watkins[6] and L. Zeng[8]

[1] University of California, San Diego, La Jolla, CA 92130, United States of America
[2] Lawrence Livermore National Laboratory, Livermore, CA 94550, United States of America
[3] ITER Organization, CS 90 046, 13067 St.-Paul-lez-Durance Cedex, France
[4] University of Ljubljana, Ljubljana 1000, Slovenia
[5] General Atomics, San Diego, CA 92186-5608, United States of America
[6] Sandia National Laboratories, Albuquerque, NM 87185, United States of America
[7] University of Strathclyde, Glasgow G40 4JR, United Kingdom
[8] University of California, Los Angeles, Los Angeles, CA 90095, United States of America

E-mail: perillor@fusion.gat.com

Abstract

Type-I and type-II edge-localized-modes (ELMs) heat flux profiles measured at the DIII-D divertor feature a peak in the vicinity of the strike-point and a plateau in the scrape-off-layer (SOL), which extends to the first wall. The plateau is present in attached and detached divertors and it is found to originate with plasma bursts upstream in the SOL. The integrated ELM heat flux is distributed at $\sim$65% in the peak and $\sim$35% in this plateau. The parallel loss model, currently used at ITER to predict power loads to the walls, is benchmarked using these results in the primary and secondary divertors with unprecedented constraints using experimental input data for ELM size, radial velocity, energy, electron temperature and density, heat flux footprints and number of filaments. The model can reproduce the experimental near-SOL peak within $\sim$20%, but cannot match the SOL plateau. Employing a two-component approach for the ELM radial velocity, as guided by intermittent data, the full radial heat flux profile can be well matched. The ELM-averaged radial velocity at the separatrix, which explains profile widening, increases from $\sim$0.2 km s^{-1} in attached to $\sim$0.8 km s^{-1} in detached scenarios, as the ELM filaments' path becomes electrically disconnected from the sheath at the target. The results presented here indicate filaments fragmentation as a possible mechanism for ELM transport to the far-SOL and provide evidence on the beneficial role of detachment to mitigate ELM flux in the divertor far-SOL. However, these findings imply that wall regions far from the strike points in future machines should be designed to withstand significant heat flux, even for small-ELM regimes.

---

* Author to whom any correspondence should be addressed.

1. Introduction

Edge-localized-modes, or ELMs, are periodic plasma instabilities observed in high-confinement mode (H-mode) plasmas where particles and energy (up to ∼20% of the plasma stored energy [1, 2]) are released from the pedestal region into the scrape-off-layer (SOL) in the form of field-aligned plasma structures [3, 4]. ELMs provide density and impurity pump-out, preventing accumulation in the core [5], but lead to high transient power loads that can compromise the lifetime of the plasma-facing-components (PFC). Unmitigated type-I ELMs energy loads in ITER [6] are expected to exceed the melting threshold of the Tungsten (W) divertor PFC by a factor ~2 or more [7] and, therefore, are to be avoided.

ELM heat load mitigation strategies are currently being investigated and include, among others, (i) high-frequency low-energy ELMs [8] (ii) operating in quasi-double-null (QDN) [9] configuration to spread the exhausted power over a larger area compared to a single-null (SN), (iii) plasma detachment, where plasma pressure drops along open magnetic field lines from the outer midplane (OMP) to the target [10, 11], and (iv) suppression or mitigation of ELMs with resonant magnetic perturbations [12].

The parallel-loss-model (PLM) [13] is a fluid code that evaluates the time-averaged ELM power flux density by calculating particle and energy loss from an ELM filament due to parallel transport in the SOL. The PLM has been first benchmarked [14] with experimental measurements of type-I ELMs ion energy in the far-SOL in JET [15] and has then been used to predict ELM-induced power flux scenarios in ITER i.e. ELM power loads to the upper part of the vessel and to the first wall [16, 17] and to the front-end structures of the ICRH antennas, located at the OMP [18].

In this work, we advance the benchmarking of the PLM model by constraining all the inputs by high spatial and temporal resolution measurements for the first time and then compare the PLM-generated heat flux profiles to experimental ones under a variety of conditions. We investigate type-I and type-II (also referred to small type-I) ELMs for various divertor scenarios, together with type-I ELMs to a secondary divertor in QDN configuration. To discriminate between type-I and type-II ELM regimes, we adopt the definition provided by Snyder *et al* [8], which states that type-II ELMs occur at high pedestal collisionality where the current does not reach the peeling-balooning limit in the stability diagram but the pure ballooning limit instead, leading to a fast crash-recovery cycle where less energy is released into the SOL compared to type-I ELMs.

Furthermore, we experimentally investigate properties and propagation for ELM filaments in the SOL in these scenarios.

2. Experimental set-up

2.1. Diagnostics

Intra- and inter-ELM heat flux profiles to the outer divertor have been measured using an infra-red thermography diagnostic (IRTV, yellow in figure 1) [19], with a spatial resolution of 1.9 mm/pixel and a time resolution of 12 kHz. The view of the camera is towards the lower outer divertor and the code THEODORE [20] is used to convert surface temperatures to heat flux using temperature-dependent parameters, with an alpha value consistent with measurements made for graphite PFC (DIII-D walls).

A fast reciprocating probe (FRP) [21], located in the vicinity of the OMP, scans the edge plasma (black in figure 1), and is used here to measure SOL profiles of ion saturation current I_{sat} and floating potentials (V_f) [22]. Probe signals are digitized at 2 MHz, hence fast enough to resolve ELM fine structures. Surface Langmuir probes (LP, floor probes in figure 1) have been employed to measure intra- and inter-ELM plasma flux to the lower outer target.

A fast visible imaging system (FASTCAM in figure 1) [23], with a 2 mm/pixel spatial resolution measures photon flux from molecular Deuterium D_2^* (610 nm with 10 nm passband) from the lower divertor, and the integration times in this work vary from 0.12 to 0.5 ms. A monostatic frequency-modulated profile reflectometer [24] (orange in figure 1) measures electron density profiles during the ELMs, from which radial velocities can be extracted. Thomson Scattering measurements [25] (not shown) have been employed to extract divertor and pedestal n_e and T_e.

2.2. Discharge characteristics

DIII-D ELMy H-mode discharges are used, and in figure 2 are shown the time traces for two cases i.e. low-frequency large type-I (left) and high frequency small type-II (right) ELM scenarios. ELM and divertor characteristics are reported in table 1.

The magnetic configurations are mainly lower-SN (LSN) except the for the upper-SN (USN) and QDN, used to study the secondary divertor [26].

When an ELM occurs, D-alpha and IRTV signals peak (figure 2, blue and red) while the plasma stored energy, W_{TOT} (figure 2, orange), drops by ΔW_{ELM} i.e. the energy carried by the ELM, which is a key input parameter for the PLM.

The pedestal electron collisionality [27], ν_e^* (4th column in table 1), can influence the ELM characteristics [28, 29], where an increase in ν_e^* is associated with (i) an increase in the ELM frequency (5th column in table 1) (ii) a decrease in the normalized ELM energy (7th column in table 1) and (iii) a decrease in
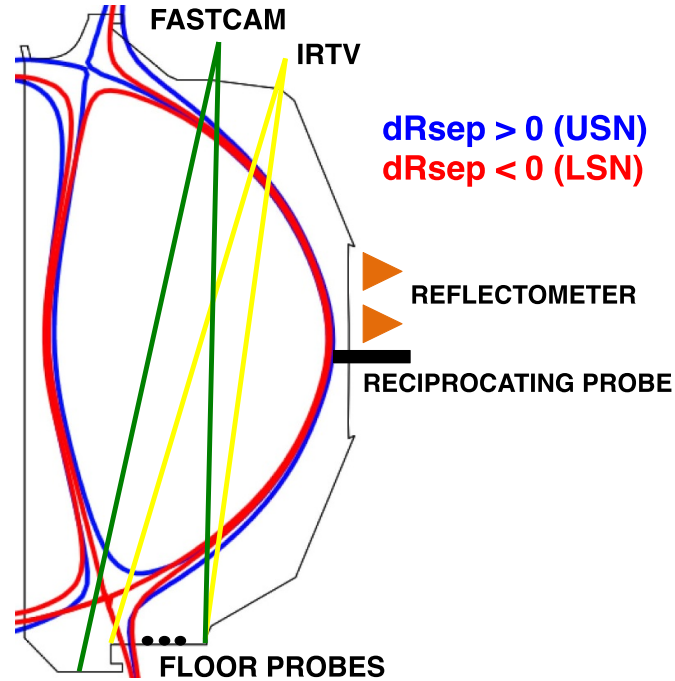
Figure 1. Diagnostics used in this work: fast camera (green), IRTV (yellow), mid-plane reciprocating probe and surface floor probes (black) and reflectometer (orange). Two representative magnetic configurations, upper-single-null (USN) and lower-single-null (LSN) are shown (blue and red, respectively).
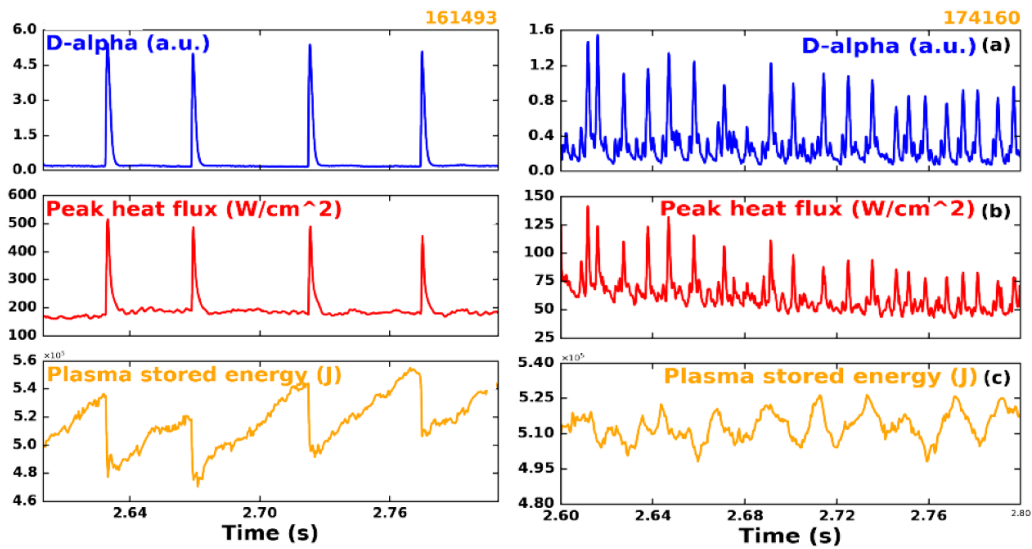
Figure 2. Time traces of D–α emission from the lower outer divertor (blue), IRTV peak heat flux at the outer strike-point (red) and plasma stored energy (orange) for two of the discharges used in this work.

Table 1. Divertor and ELM characteristics for the shots used in this work. Note that $T_{e,\,target}$ values in column 8 is inter-ELM.

Shot #	ELM type	Magnetic configuration	ν^*_e	f_{ELM} (Hz)	W_{ELM} (kJ)	$\Delta W_{ELM}/W_{TOT}$ (%)	DTS $T_{e,target}$ (eV)	Divertor condition
161 493	I	LSN	1.5	20	53	9.5	28	Attached
176 346	I	LSN	2.5	35	43	6.5	10	High-recycling
174 262	I	LSN	3.1	60	35	5	3–5	Partially detached
174 160	II	LSN	5.2	135	15	2.5	0.8–1.5	Detached
135 929	I	USN/QDN	1	35	70	9	32	Attached
135 930								(secondary
135 932								divertor)

Table 2. Main steady-state plasma parameters for the shots used in this study.

Shot#	$<n_e>/n_{GW}$	P_{inj} (MW)	$P_{rad,\,tot}$ (MW)	P_{SEP} (MW)
161 493	0.48	2.6	0.9	2.25
176 346	0.61	2.6	1.6	2.5
174 262	0.7	4.5	2.8	4
174 160	0.78	4.9	3.6	3.5
135 929 135 930 135 932	0.43	3.5	—	—

the inter-ELM electron temperature at the target, $T_{e,\text{target}}$ (8th column in table 1). ν^*_e is also often connected with divertor conditions [30].

In this work we study ELMs power flux to the divertor for attached, high-recycling, partially detached and detached divertors (9th column in table 1). For a detailed description of these regimes, the reader is referred to the reviews carried out by Leonard [10] and Krasheninnikov *et al* [31]. The degree of detachment, described in [32] and often used to quantify plasma detachment, is ~1.8 for the partially detached case and ~3.5 for the detached one.

The main steady-state plasma parameters for the shots adopted in this work are listed in table 2, where $<n_e>/n_{GW}$ is the Greenwald fraction, P_{inj} the injected power, $P_{rad,tot}$ the total (plasma core, SOL and divertor) radiated power and P_{SEP} the power crossing the separatrix. Note that the radiated power from the core is not available for shots 135929-32.

3. Parallel loss model and experimental inputs

In the PLM, the energy loss rate of an ELM filament $\left(\frac{dW_{fil}}{dt}\right)$ is computed with a fluid transport code [13] which solves the conservation equations of energy and mass, averaged over an ELM filament, i.e.:

$$
\begin{aligned}
\left(\frac{\partial}{\partial t} + \frac{1}{\tau_n}\right) n &= S_n \\
\left(\frac{\partial}{\partial t} + \frac{1}{\tau_{\varepsilon,i}}\right) \varepsilon_i + \frac{\varepsilon_i - \varepsilon_e}{\tau_{ie}^{eq}} &= S_i \\
\left(\frac{\partial}{\partial t} + \frac{1}{\tau_{\varepsilon,e}}\right) \varepsilon_e - \frac{\varepsilon_i - \varepsilon_e}{\tau_{ie}^{eq}} &= S_e,
\end{aligned}
\tag{1}
$$

where n and ε are the average particle and energy densities of the filament. The removal times τ_n, $\tau_{\varepsilon,i}$ and $\tau_{\varepsilon,e}$ govern the parallel losses, and ion and electron temperatures are coupled via the electron-ion equilibration time τ_{ie}^{eq}.

The model is implemented with a modified sheath limited regime, where the parallel Mach number $M = 1$ is imposed and the sheath heat transmission coefficients for ions and electrons, γ_i and γ_e, evolve according to parallel dynamics of heat diffusivity and collisionality (further details can be found in section 5 of [13]). However, dissipative mechanisms at the divertor, typical for detached scenarios, such as plasma radiation and plasma interaction with neutrals, are not included in the code.

The ELM filament energy loss is converted to an equivalent parallel heat flux density via the equation:

$$
q_{\parallel,fil}\left(\Delta r_{sep}^{OMP}, z, t\right) = -\frac{1}{2}\frac{dW_{fil}}{dt}\frac{1}{2\pi \sigma_r \sigma_z} e^{-\frac{\left(\Delta r_{sep}^{OMP} - t v_r\right)^2}{2\sigma_r^2}} e^{-\frac{\Delta z^2}{2\sigma_z^2}}
\tag{2}
$$

where v_r is the filament radial velocity, while σ_r and σ_z are the filament half-width of a Gaussian profile structure in r and z coordinates, and have been obtained from beam emission spectroscopy measurements, previously published [33], and FRP measurements via the relation $\sigma_r = v_{r,ELM\_fil}\Delta t_{ELM\_fil}$; in this study, σ_r and σ_z vary between 0.25–0.75 cm and 1–2 cm, respectively. These measurements are also consistent with previous simulations [34] showing σ_r being roughly the pedestal half-width.

In the PLM, filaments are assumed to originate at the OMP and to travel in the radial direction with parallel losses and without poloidal spreading or fragmentation. The averaged filament energy is given by:

$$
E_{\parallel,fil}\left(\Delta r_{sep}^{OMP}\right) = \int q_{\parallel,fil}^{OMP}\left(\Delta r_{sep}^{OMP}\right) dt
\tag{3}
$$

which allows for the calculation of the time-averaged ELM heat flux profile at the OMP, assuming toroidal symmetry and accounting for the ELM frequency, as:

$$
q_{\parallel,ELM}^{OMP}\left(\Delta r_{sep}^{OMP}\right) = \frac{E_{\parallel,fil}\left(\Delta r_{sep}^{OMP}\right) f_{ELM}\sigma_z n_{fil}}{\pi R_{OMP}\left(\frac{B_\theta}{B_\phi}\right)}
\tag{4}
$$

where $E_{\parallel,fil}\left(\Delta r_{sep}^{OMP}\right)$ is the filament-averaged energy in each radial location, f_{ELM} is the ELM frequency (table 1), n_{fil} is the ELM number of filaments (which will be discussed later in this Section), B_θ and B_ϕ the poloidal and toroidal magnetic field, respectively.

The time-averaged perpendicular ELM power flux density to the divertor PFC, accounting for magnetic flux expansion, is then calculated as:

$$
q_{\perp,DIV} = \frac{R_{OMP}}{R_{DIV}} q_{\parallel,ELM}^{OMP}\left(\Delta r_{SEP}^{OMP}\right) \sin\alpha
\tag{5}
$$

where R_{OMP} and R_{DIV} are the radial positions at the OMP and divertor target, respectively, and α is the total angle between the incident magnetic field lines and the target surface, typically around 2–3 degrees.
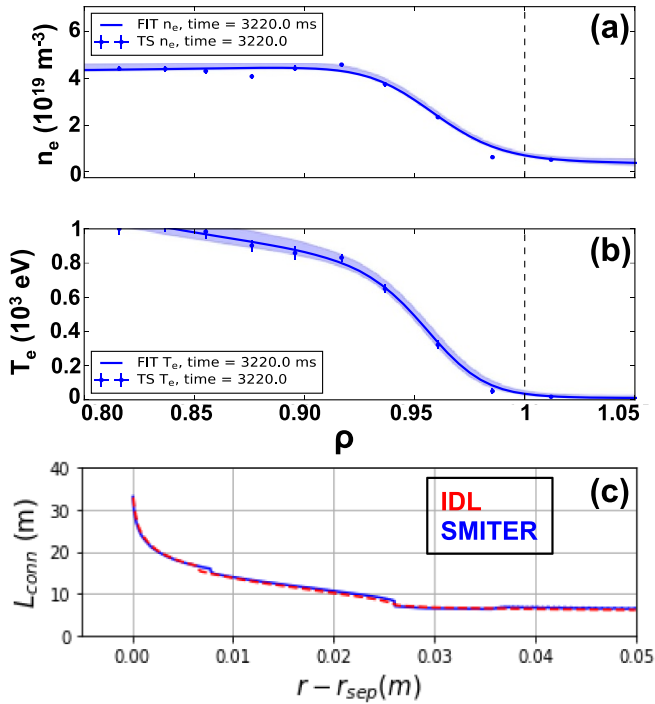
Figure 3. (*a*) Electron density and (*b*) electron temperature profiles for a representative shot adopted in this study (#135932) (*c*) L_{conn} at the OMP from SMITER and EFIT-IDL (#135932, EFIT01, $t = 2180$).

The inputs needed by the PLM are constrained by using experimental measurements and numerical tools as follows, i.e.:

(i) Initial T_{e} and n_{e} of the filaments at the OMP, which are extracted from TS measurements of the pedestal profiles (a representative case is shown in figures 3(*a*) and (*b*)). To address the filament's origin in the pedestal, we carried out a sensitivity study which will be shown later in the paper. In the model, quasi-neutrality is assumed i.e. $n_{\mathrm{e}} = n_{\mathrm{i}}$, and the main ion temperature, $T_{\mathrm{i}}^{\mathrm{D}+}$, is set $\sim 1.5^{*}T_{\mathrm{e}}$, in accordance with measurements in ASDEX-Upgrade [35], DIII-D [36] and JET [37].

(ii) The connection lengths, L_{conn}, i.e. the distance along the field lines between the OMP and the outer target, have been obtained by IDL codes from EFIT reconstructions [38] and also benchmarked with the 3D field line tracing code SMITER [39], showing agreement within $\sim 5\%$ for all cases examined (an example is reported in figure 3(*c*)).

(iii) The ELM energy, ΔW_{ELM}, is obtained by conditional averaging the ELM-driven drop in the diamagnetic loop signal of the plasma stored energy (orange in figure 2) over ~ 30 ELMs. In this work, considering type-I and type-II ELMs, ΔW_{ELM} values are between 15 kJ and 70 kJ.

(iv) The radial velocity of the filament, v_r in equation (2), is measured at the OMP and allows modeling of the radial evolution of the filament. ELM v_r profiles are extracted from FRP measurements via the relation $v_r = \frac{E_\theta \times B}{B^2}$, where

E_θ is derived from V_{f} measurements at two poloidally-separated tips as $E_\theta = -\frac{V_{\mathrm{f,2}} - V_{\mathrm{f,1}}}{d}$, where d is the distance between the two tips. Figure 4(*a*) shows the FRP-measured ELM radial velocity (red), together with the probe's movement (black) and D–α emitted from the lower outer divertor (blue). For standard PLM runs, v_r input to the code has been obtained by averaging the FRP $E \times B$ measurement over the whole ELM, using D–α as reference, and the resulting peak velocities for several ELMs in the SOL have been fitted with an exponential of the form $v_r = v_{r,\mathrm{peak}} e^{-\left(\frac{R - R_{\mathrm{MID}}}{\lambda_v}\right)}$. However, ion saturation current signals, indicated by I_{sat} in figure 4(*b*) for a single ELM event, reveal several small peaks with radial velocities in the range between $0.2\,\mathrm{km\,s}^{-1}$ to $\sim 2\,\mathrm{km\,s}^{-1}$ (red in figure 4(*b*)) i.e. varying by a factor ~ 10. To evaluate the velocity of such small structures, v_r is smoothed using a low-pass filter that preserves the features of the structures' time scale, as observed in the I_{sat} signal (figure 4(*c*)). This temporal feature will be accounted for, and it will be discussed later in the paper where we account for two velocity components in the simulations.

Reflectometry can also be used to measure ELM peak v_r by tracking the evolution in the density profile with time [24] and yielding a velocity vs time trace. Here, we have used reflectometry measurements only for the type-I attached case, where FRP data were not available.

(v) The number of filaments, n_{fil} in equation (4), has been estimated by the code ELITE [40], which evaluates the stability of the pedestal region for intermediate to high toroidal mode number instabilities ($n \sim 5$–35). The output for the attached LSN type-I ELM case is shown in figure 5, showing a toroidal mode $n = 10$ right before the ELM crash. Here, we assume the toroidal modes n to evolve as ELM filaments, n_{fil} (note that toroidal averaging is assumed in the PLM). For the scenarios studied in this work, n_{fil} ranges between 6 and 25.

4. Experimental results

The PLM and its inputs have been described in section 3, while in this section experimental measurements and analysis are presented on type-I and type-II ELM heat flux deposition to the floor and filaments' propagation in the SOL for various divertor conditions.

4.1. Type-I ELM heat flux profiles in attached divertor

A typical IRTV ELM peak heat flux as a function of time is shown in figure 6(*a*) for a well-attached divertor condition, where each point is the maximum extracted from a profile that extends in radius over the lower outer divertor (inset in figure 6(*a*)).

Time-averaged ELM heat flux profiles, which will be compared to PLM outputs in section 5, have been obtained by conditional averaging IRTV data over ~ 30 ELMs, as shown in in figure 6(*b*) for the case of type-I ELMs on attached divertor
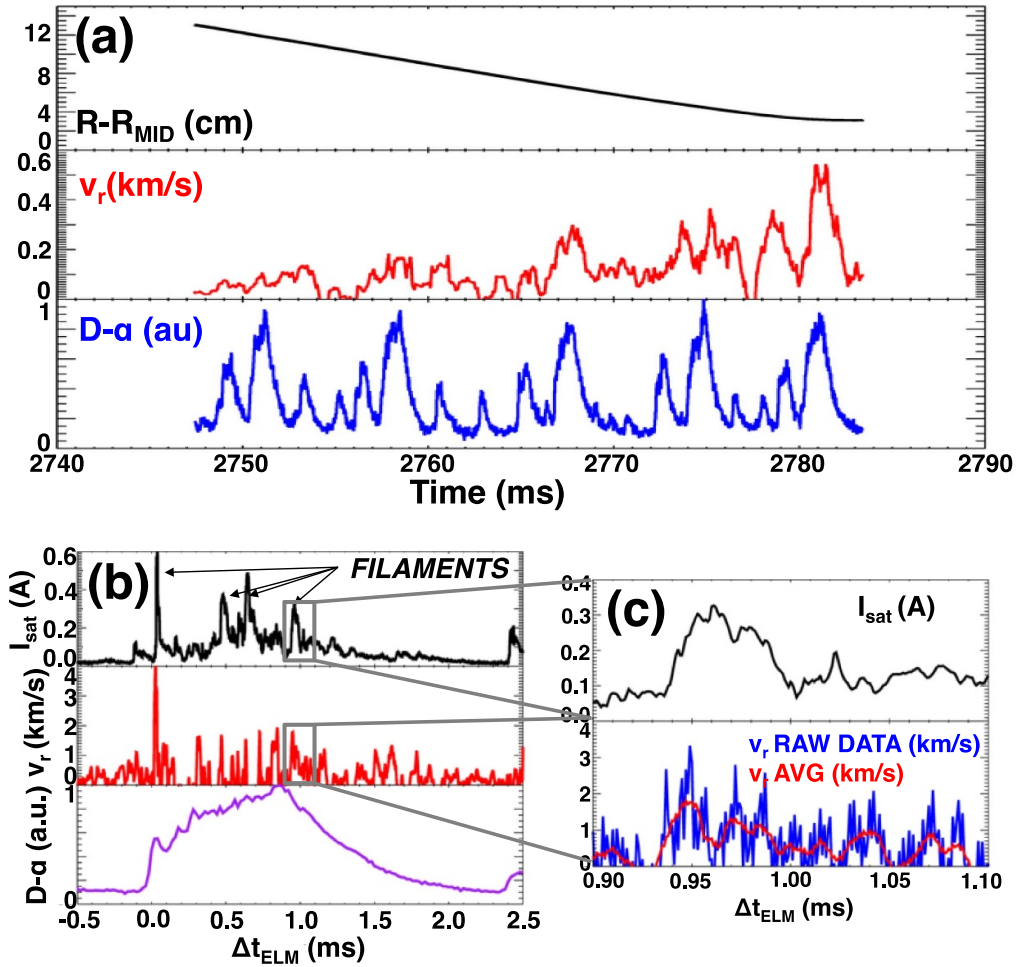
Figure 4. (*a*) FRP signals measured for shot #174160, showing the probe penetration (black), the ExB velocity, which allows to obtain the radial velocity of the ELMs from the peaks (red), and D–α emission from the lower outer divertor, measured with filterscopes (blue). (*b*) FRP measurements of I_{sat} (black), v_r (red) and D-alpha from the lower outer divertor (purple) for a single ELM. (*c*) FRP measurement of I_{sat} (black), raw v_r data (blue) and smoothed v_r (red) of a single ELM filament.
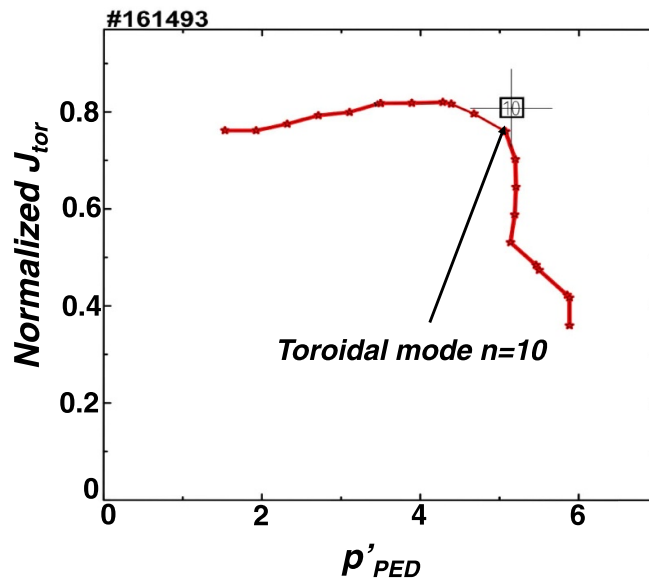

Figure 5. Pedestal stability diagram generated from ELITE for shot #161493, showing the toroidal mode number $n = 10$.
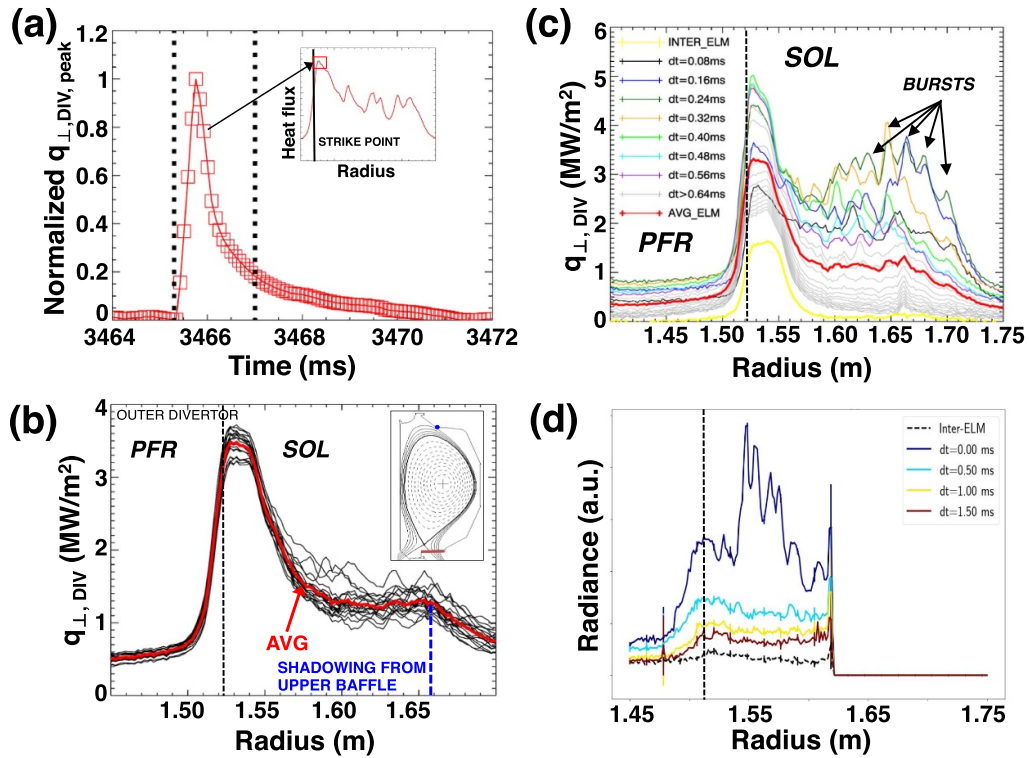
Figure 6. (*a*) Normalized perpendicular peak heat flux VS time for a typical ELM with a well attached divertor (#161493), measured at the lower outer divertor. The two black dotted lines indicate the time window used to average in time and the inset shows a representative instantaneous heat flux radial profile for a specific time. (*b*) Conditionally averaged heat flux (red) over ∼30 ELMs (black). The inset shows the divertor region where the IRTV measurements are taken at the floor (dark red) and the upper baffle (blue). (*c*) Time evolution for a typical type-I ELM VS radius in attached divertor. The averaged profile, in red, shows a plateau in the far-SOL. (*d*) Radiance vs time before and during a typical ELM of the ones examined in this shot; note that, for this case, the view of the fast camera is up to radius ∼1.62 m and that the time integration is 0.5 ms, yet enough to detect bursts in the far-SOL.

(#161493). The ELM time window ends when the normalized peak heat flux vs time decreases by 2 e-folding times of the maximum (black dotted lines in figure 6(*a*) mark our definition of the beginning and the end of a typical ELM). Note that the conditionally-averaged profile, in red in figure 6(*b*), shows a plateau in the far-SOL, before decreasing further once the field lines encounter the flux line connected to the baffle in the upper vessel (blue in figure 6(*b*)). The time evolution of a typical type-I ELM profile at DIII-D is shown in figure 6(*c*), featuring the plateau in the averaged profile (red) and bursts (or flashes) during the ELM duration that extend radially over the whole outer divertor. Such features are similar to the ones observed in both primary and secondary attached divertors for type-I, type-II and grassy ELMs [41]. Reflection effects may be a concern for IRTV measurements; however, this effect is expected to be strongly reduced in carbon wall machines compared to metal wall ones [42], due to the the low emissivity of e.g. W ($\varepsilon \sim 0.2$–0.3) compared to graphite ($\varepsilon \sim 0.8$–0.9). Possible reflection effects have been accounted for in this work by subtracting to the IRTV profiles the heat flux measured in the PFR and far-SOL during inter-ELM.

The FASTCAM radiance profile time evolution is shown in figure 6(*d*), where burts in the divertor SOL can be

observed and they extend throughout the whole view of the camera. D_2^* can be used as a proxy for the particle flux, as discussed in [43]. The errors, indicated with vertical lines in figure 6(*d*), are the standard deviation of the radial radiance profiles averaged toroidally over ∼1° and are consistent with Poisson statistical analysis of error propagation. The magnitude of the errors is not significant when compared to the bursts, which excludes those features to be artifacts of the measurement.

Figures 6(*c*) and (*d*) show measurements for the same ELM. Note that FASTCAM view and IRTV in DIII-D are in different toroidal locations.

ELM bursts in the far-SOL, first reported in ASDEX-Upgrade [44], were characterized by heat flux magnitude ∼15 times lower compared to that at the peak near the SP, and were interpreted as ELM filaments moving coherently along open magnetic field lines and depositing power via parallel transport. Here, however, we observe bursts depositing heat flux into the far-SOL region of the divertor that are comparable, or larger, than that at near the SP. This is in line with IRTV measurements of type-I ELMs taken at JET and reported in [45–47], which were interpreted as 'strike point jumps' due to the effect of the ELM current on the magnetic topology of the separatrix.

4.2. Type-I ELM heat flux footprints in partially detached divertor

The heat flux footprint for type-I ELMs in partially detached divertor conditions is shown in figure 7(*a*), for a representative ELM, where a significant fraction (∼30%) of the time-averaged heat flux (in red) reaches the far-SOL i.e. from Ψ_n from ∼1.03 (radius ∼ 1.51 m) and outside. ELM plasma reaching that region is confirmed by measurements of ion saturation current (I_{sat}) from an array of floor LP covering the outer divertor shelf up to radius =1.66 m, shown in figure 7(*b*). Note that, during the inter-ELM period, I_{sat} is significant (∼0.4 A) only at the probe at $\Psi_n = 1.03$ i.e. radius ∼ 1.49 m.

Here, bursts in the far-SOL are not observed with IRTV, in contrast with the attached case shown in figure 6(*b*). However, measurements of D_2^* radiance viewing vertically down from the top of the vessel into the lower divertor (figure 7(*c*)) reveal distinct flashes in the early phase of the ELM, followed by a homogeneous emission throughout the volume above the target, suggesting that bursts dissipate before reaching the floor. A possible explanation might be related to plasma-neutrals interaction, with the filaments that thin out via charge-exchange, ionization, ion-conversion and recombination, resulting in a ∼uniform power deposition pattern, as expected from a dissipative divertor. Dedicated simulations with e.g. SOLPS [48] would be needed to underline the relative importance of such volumetric mechanisms.

4.3. Type-II ELM heat flux footprints in detached divertor

The power deposition during type-II ELMs to a detached divertor, which is expected to differ significantly from an attached case, is evaluated. Figure 8(*a*) shows the temporal heat flux evolution of a representative type-II ELM, where it can be noted that (i) the instantaneous peak heat flux at d$t = 0.56$ ms (in purple) is ∼3 times that of the inter-ELM period (in yellow) (ii) the inter-ELM profile does not decay to zero up to radius ∼1.64 m (Ψ_n ∼ 1.07) and (iii) the ELM-averaged profile (red in figure 8(*a*)) shows a plateau in the divertor far-SOL throughout the region from $\Psi_n = 1.02$ (radius ∼ 1.55 m) to $\Psi_n = 1.1$ (radius ∼ 1.70 m).

It has been previously shown [41] that the heat flux footprint of attached type-II ELMs display bursts in the far-SOL with values higher than that at the SP; however, those bursts are not measured at the target surface in detached scenarios (figure 8(*a*)). Figure 8(*b*) shows a FASTCAM 2D frame (d$t_{ELM} = 0.2$ ms), where distinct structures extending over the SOL can be seen, while figure 8(*c*) reports the FASTCAM radiance profile evolution during the ELM and shows bursts that last ∼0.6 ms. These experimental observations, which are in line with what we observe for type-I ELMs in partially detached conditions (section 4.2), provide support to the beneficial role of partially detached and detached regimes for ELM heat flux mitigation in regions of the divertor
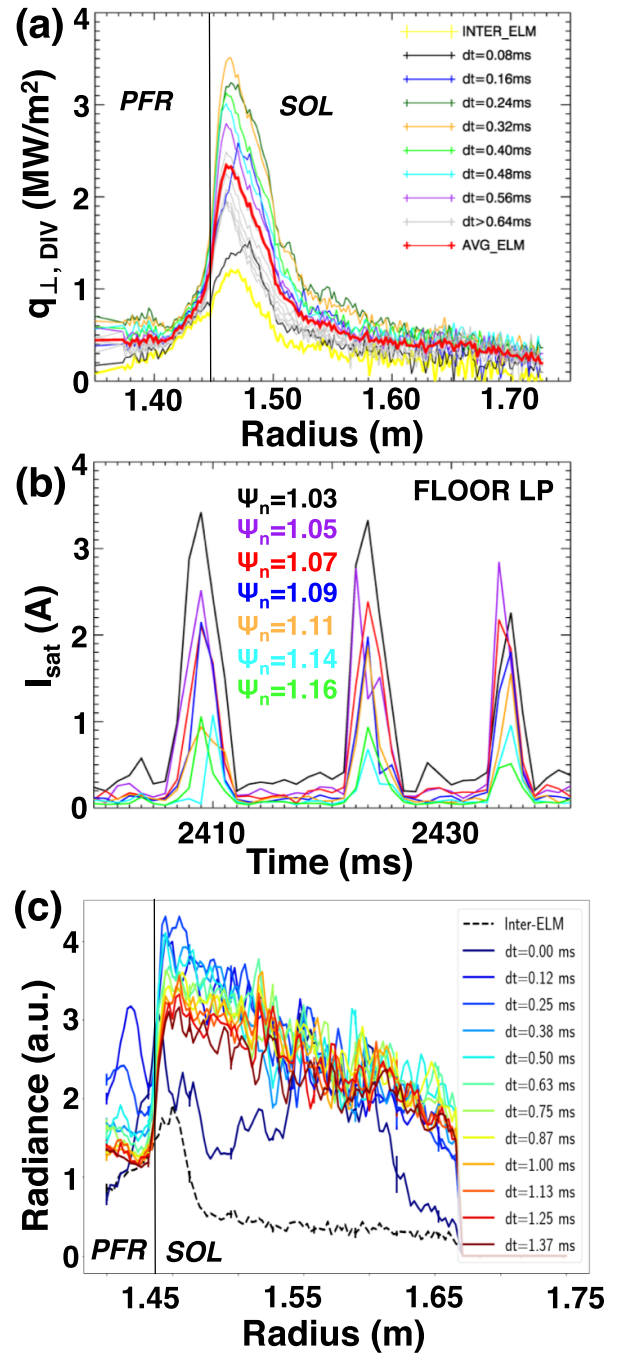
far from the strike-point. However, the near-SOL divertor heat flux increase during the ELM indicates that plasma burns through the detachment layer [49] also in the case of small ELMs.

Figure 7. (*a*) Heat flux profile evolution of a type-I ELM in partially detached divertor (#174262). Profiles are taken every 0.08 ms (in color) and the time-averaged profile is indicated in red. (*b*) I_{sat} measurements by floor Langmuir probes in the lower outer divertor. The inset shows the location of the probes. (*c*) Radial profile of D_2^* emission for the same ELM, measured with the fast camera. Profiles are taken every 0.12 ms, with the inter-ELM one indicated with a dashed black line, and the errors are indicated with vertical lines every ten points in the profiles.
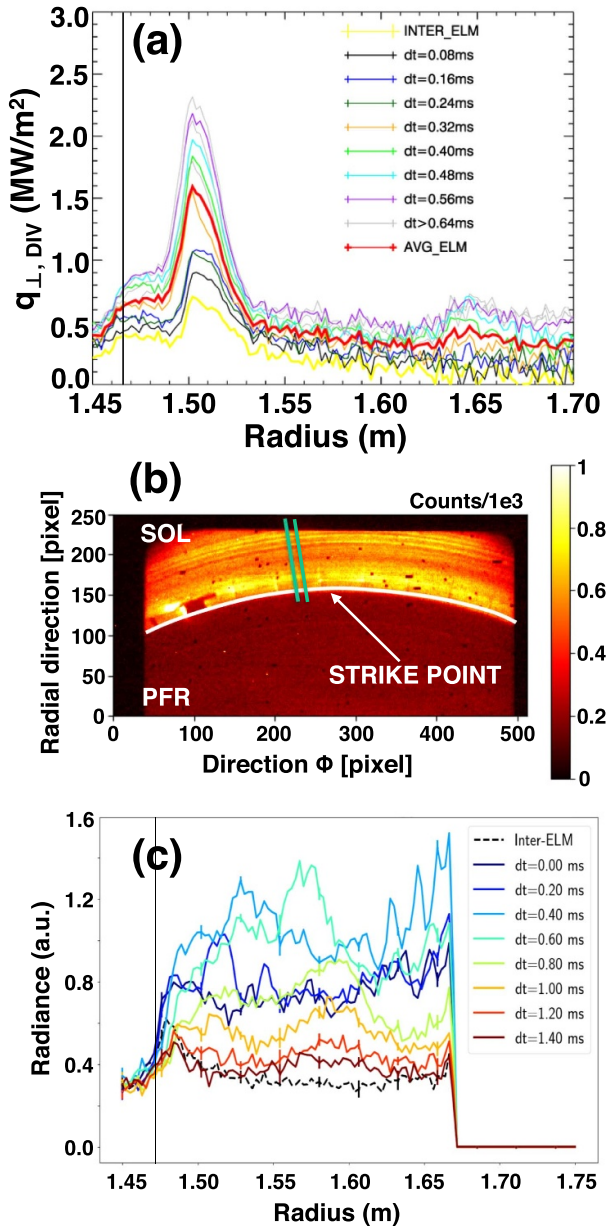
Figure 8. (*a*) Single type-II ELM heat flux profile evolution in detached divertor (#174160). Profiles are taken every 0.08 ms (in color), and the time-averaged profile is indicated in red. (*b*) Fast camera 2D frame (top view, D_2^* filter) taken during the ELM at $dt_{ELM} = 0.2$ ms. The region from which the radial profiles are extracted is indicated in green. (*c*) Time evolution of the ELM radiance from the divertor.

4.4. Radial velocity of ELM filaments for various divertor conditions

The ELM radial velocity is an important parameter that influences the divertor heat flux profile widening and the fraction of ELM power that reaches the first wall. Furthermore, the filaments' v_r is an important input parameter for the PLM, as shown in equation (2).

Measurements on ELM radial velocities in the literature have shown values ranging from ~0.07 km s^{-1} in K-STAR [50] to 2–3 km s^{-1} in ASDEX-Upgrade [51], NSTX [52]

and MAST [53], and intermediate values (0.2–0.7 km s^{-1}) observed in JET [15] and DIII-D [33]. The velocity profiles input to the model and examined in this work, shown in figure 9(a), are obtained by fitting the peak radial velocities of the ELMs (typically 2–3 ELMs per case, as shown in red for the partially detached case), measured through the SOL with FRP, with an exponential function, as discussed in section 3, except for the attached case (in black) which is measured with reflectometry and whose decay length is extracted from a sensitivity study that will be discussed in section 5.1.

Note that for the type-II ELM case we fit the velocities of ~15 ELMs, being those high frequency hence allowing the probe to measure a higher number of ELMs in a single reciprocation.

The ELM peak radial velocities in figure 9(*a*) range from ~0.2 km s^{-1} up to to ~0.8 km s^{-1} in attached and detached conditions, respectively, consistent with previous DIII-D measurements [32]. The radial velocity decay length, λ_v, varies from ~25–30 cm for attached, high-recycling and partially detached scenarios to ~16 cm for the detached one. Such a difference might be related to the effect of neutral distribution, which leaks from the divertor and can vary significantly during detachment. This has been qualitatively verified by comparing the same filterscope D-alpha signal at the OMP (not shown), which go from 1.6×10^{12} ph cm^{-2} sr^{-1} s^{-1} in the attached case to ~3.2×10^{13} ph cm^{-2} sr^{-1} s^{-1} in the detached one.

It has been theoretically [54] and experimentally shown [55] that the $E \times B$-driven radial evolution of filaments (or blobs) is connected with the collisionality in the divertor. Here, we have explored those findings in the context of ELM filaments for the discharges used in this work. The peak filaments radial velocity at the separatrix (R–$R_{mid} = 0$ cm), reported in figure 9(*b*), increases as the ELM filaments path becomes electrically disconnected from the sheath at the target as the normalized collisionality in the divertor, Λ_{DIV}, increases. Λ_{DIV} is calculated as in [56]:

$$\Lambda_{DIV} = 1.7 \times 10^{-14} \frac{n_e L_{conn}}{T_e^2} \qquad (6)$$

where T_e (eV) and n_e (cm^{-3}) are measured with DTS at ~8 cm from the floor, corresponding to $\Psi_n \sim 1.015$, and L_{conn} (cm) is the connection length from the DTS location of the measurement to the floor. Note that these shots have a similar shape.

The data presented in figure 9(*b*) are consistent with the theory of convective transport in the SOL by intermittent filaments [57, 58] i.e. magnetic field gradient leads to charge separation inside the filament, resulting into $E \times B$-driven cross-field radial motion. ELM filaments are therefore expected to travel in radius at higher velocity in detached conditions because they cannot discharge to the target fast enough due to high collisionality (and resistivity) in the divertor. A more expanded work, which will evaluate ELM filaments radial velocity in both OMP and divertor simultaneously, together with the interplay between upstream SOL vs divertor SOL conditions, is currently ongoing and will be published in a future paper.
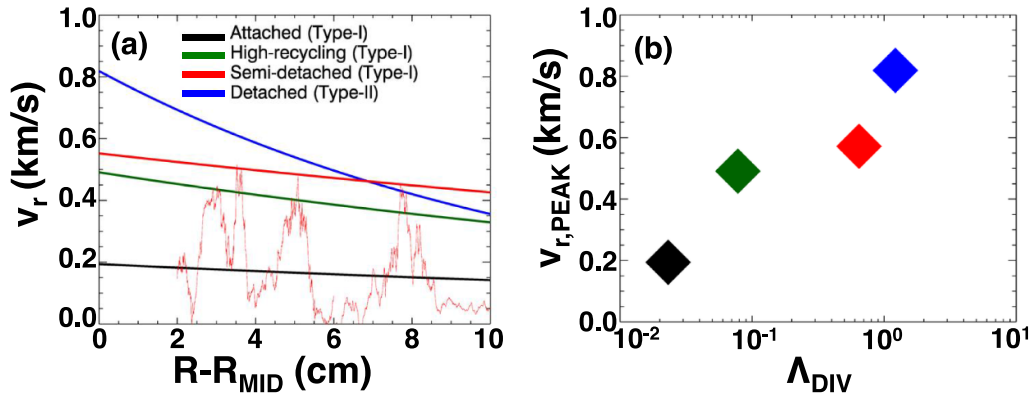
Figure 9. (*a*) Fitted ELM radial velocity profiles vs R–R_{mid} for the cases examined in this work, with three ELMs from the partially detached case shown for reference and (*b*) peak ELM radial velocities measured at the separatrix VS normalized collisionality in the divertor Λ_{DIV}, with the same color code.

5. PLM simulations of ELMs and comparison with experiments

Having discussed the various experimental measurements and how the inputs to the PLM are constrained, in this section we proceed to compare PLM simulations with time-averaged type-I and type-II ELM heat flux measurements at the floor for various divertor scenarios.

5.1. PLM simulations of type-I ELM heat flux to the primary divertor

We first evaluate the PLM sensitivity to: (i) ELM filaments radial velocity decay length λ_{v} (figure 10(*a*)) and (ii) filaments' location of origin in the pedestal (figure 10(*b*)) by running the model and scanning the relevant parameter while leaving the others constant. The peak radial velocity for these ELMs, 0.191 km s^{-1} i.e. equal to the value measured at the separatrix in well attached conditions as shown in figure 9, has been obtained from reflectometry measurements. The scanned radial velocity decay length, λ_{v}, is scanned between 0.03 and 0.32 m in five steps. The resulting radial velocity profiles corresponding to the selected decay lengths are shown in figure 10(*a*) and used as input to separate PLM cases. Initial filaments' n_{e} and T_{e} (measured by TS) are also input into the PLM cases for three separate locations in the pedestal as taken from the same attached divertor discharge, and plotted vs ρ in figure 10(*b*).

The PLM simulation results are then compared with the actual IRTV profile measured in the discharge, as shown in figures 10(*c*)–(*e*). This comparison reveals that the peak power flux is not quite sensitive to the input values of T_{e} and n_{e}, while the width of the profile is influenced by λ_{v}. The PLM runs that match the experimental profile is best characterized by initial T_{e}, n_{e} from the mid-top pedestal, in figures 10(*d*) and (*e*), with $\lambda_{\mathrm{v}} = 0.32$–$0.22$ m. We will therefore use the values of T_{e} and n_{e} taken between the mid and top pedestal as input to the code from here on. The profile peak could be matched well, within 5%, if the ΔW_{ELM} input to the PLM would be increased by

$\sim$5 kJ, i.e. $\sim$10% more than what the diamagnetic loops data indicate for these ELMs.

The PLM-IRTV heat flux profile comparisons for attached, high-recycling and partially detached divertor regimes, featured in figures 11(*a*)–(c), show that the model reproduces the experimental near-SOL peak heat flux value, within $\sim$20%, which is an important parameter for divertor design and engineering, but does not reproduce the plateau. The radial velocity profiles input to the model are shown in figure 9(*a*) of section 4.4. Note that PLM predictions under-estimate the full power load to the divertor, but that it mostly does so in the far-SOL, where the divertor is designed for lower heat loads. The error bars, shown in each plot, are the averaged RMS values.

5.2. ELM plasma transport to the far-SOL and composite PLM modeling

There are multiple theoretical explanations for the bursty ELM filamentary characteristics, which might lead to the experimental observations made here.

Simulations of ITER-like ELMs ($\Delta W_{\mathrm{ELM}} \sim 4$ MJ, $\nu^{*}_{\mathrm{e}} \sim 0.08$) with the code JOREK have shown [34] that the origin of the far-SOL heat flux footprint can be related to changes in the magnetic topology of the plasma edge, where the field perturbation driven by the ELM causes an ergodization of the core edge magnetic field, forming so-called homoclinic tangles. The magnetic field lines inside the tangles start in the core and are connected to the target, forming multiple peaks in the divertor heat flux radial profile and spirals in the toroidal direction.

On the other hand, modeling with BOUT [28] and BOUT++ [59] shows that the formation of filaments is associated with the convective motion of the ballooning modes across the separatrix. These filaments burst explosively during the non-linear phase of the ELM [60] and propagate rapidly in radius, carrying particles and energy across the LCFS which are then lost via parallel transport. In the SOL, filaments develop dipolar (equal and opposite in both poloidal directions) vorticity and electrostatic potential fields, leading to flute-like instabilities [61] that result in the formation of a
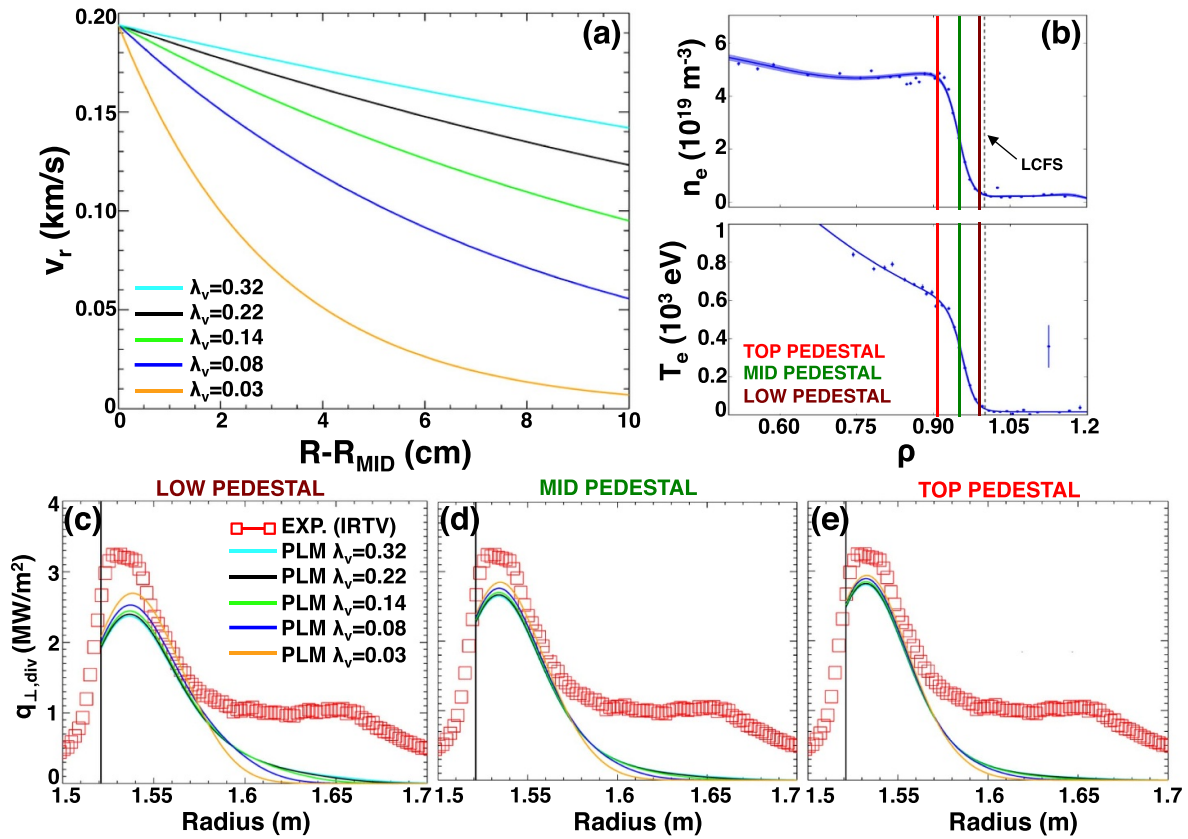
Figure 10. (*a*) Virtual ELM radial velocity profiles at the outer midplane used as input for PLM modeling. (*b*) Electron temperature and density profiles measured by TS in the main SOL showing three different pedestal origins for the filaments i.e. top (red), mid (green) and low (brown) pedestal. (*c*)–(*e*) PLM-IRTV comparison with various radial velocities and low, mid and top pedestal values of n_e, T_e as initial parameters.
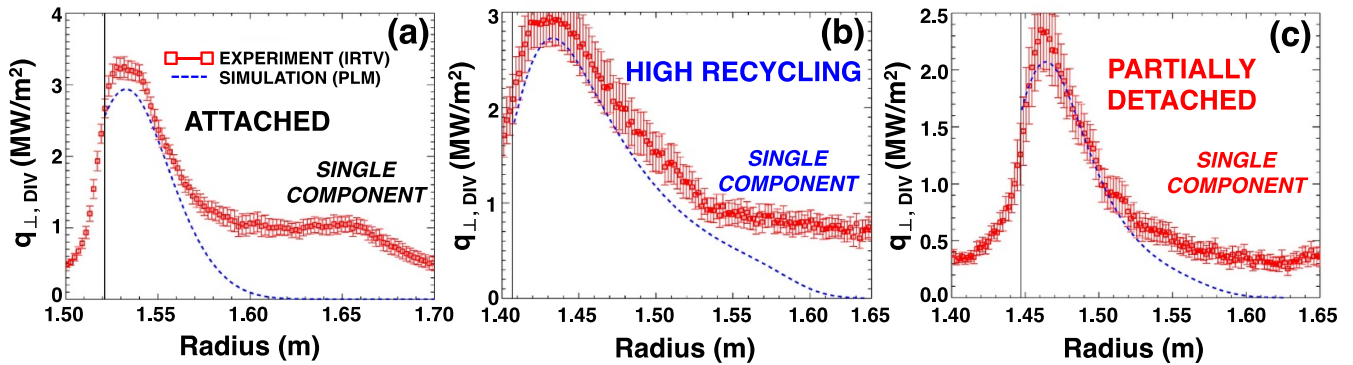

Figure 11. (*a*)–(*c*) IRTV-PLM comparison with single PLM runs carried out for attached, high-recycling and partially detached discharges. The PLM reproduces the peak, within ~20%, but fails to match the plateau.

steep front and a trailing wake [17]. This mechanism [56] can cause the filaments to break into smaller ones (so-called filament fragmentation), resulting in structures characterized by varying radial velocities that can carry a significant fraction of the ELM energy to the far-SOL.

Experimental data from various machines have shown that ELMs are composed of discrete structures [15, 33, 62–64] that vary in dimension and radial velocity. The concept of small filaments moving quickly in radius is supported by analytical theory of filaments (or blobs) radial transport in the SOL [56],

which shows that the normalized velocity, $\hat{v}_r$, scales inversely with the normalized filament radius $\hat{a}$ i.e. $\hat{v}_r \propto 1/\hat{a}^2$.

Although it is not clear yet whether such structures result from fragmentation of larger filaments, we have explored such possibility by carrying out two separate PLM runs per each ELM case, dividing the ELM into a 'slow' and a 'fast' radial velocity component and then adding up the two resulting profiles in order to attempt to better match the heat flux profile in the far SOL. The fast component for these PLM runs has v_r between 1.5 km s^{-1} and 2.5 km s^{-1}, which
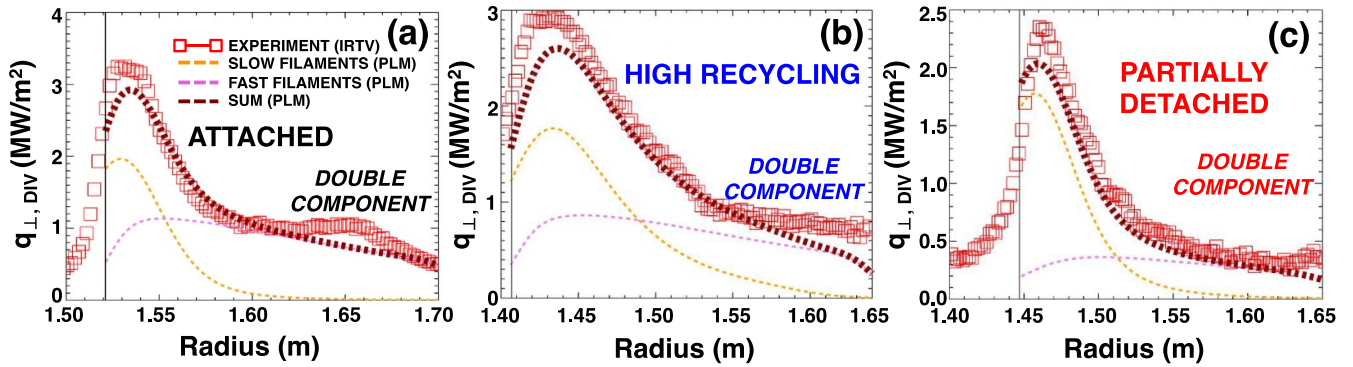
Figure 12. (*a*)–(*c*) IRTV-PLM comparison with two separate PLM runs, indicated as Slow and Fast (orange and pink, respectively); the sum of the two runs (brown), reproduces the experimental profile averaged over the ELM cycle for 30 ELMs during each divertor condition within 15%.

is consistent with our measurements, (see the example in figure 4(*c*)) and the ELM energy, ΔW_{ELM}, is split among the two runs according to the ratio of the radially-integrated divertor IRTV power deposition in far- and near-SOL i.e. $\int q_{\perp,\text{FAR}-\text{SOL}} dr / \int q_{\perp,\text{NEAR}-\text{SOL}} dr$ which is evaluated to be ~35% and ~65%, respectively.

The number of filaments, which constitutes a free parameter for the fast ELM component, is set to be three times the slow component one. The fast filaments' dimensions are ~3–5 times smaller than in the standard PLM run, and are extracted from the fine structures of fast filaments measured with the FRP.

The resulting PLM profiles, indicated with a dashed brown line in figures 12(*a*)–(*c*), reproduce the experimental peak heat flux, within ~20% and the plateau. The radially-integrated power of the simulated profiles is above 80% of the experimental ELM-time averaged one. Note that the simulated profiles are temporally and toroidally averaged and, therefore, single filaments or fragments leading to instantaneous heat flux bursts in the far-SOL (as shown in the experimental data in figure 6(*c*)) cannot be modeled.

The two-component analysis shown here is in line with the theory of filaments fragmentation due to interchange instabilities, where filamentary structures originating at the mid or top of the pedestal break into smaller ones when they move radially into the SOL [65].

5.3. PLM simulations on type-II ELMs to a detached primary divertor

The conditionally-averaged IRTV type-II ELM profile is compared with the standard (or single run) PLM output in figure 13 (left). The inputs for this small ELMs case, which are obtained with the methods described in section 3, are $\Delta W_{\text{ELM}} = 15$ kJ, $n_{\text{fil}} = 25$, n_e and T_e of 3.5×10^{19} m^{-3} and 188 eV, respectively.

Although the peak value of the simulated profile is somewhat close to the experimental one, the profiles disagree significantly in both near- and far-SOL. This discrepancy might be due to (i) ELM heat flux dissipated into the far-SOL

divertor region via plasma-neutrals interaction (ii) molecular lines affecting the measurement [66], (iii) the fact that the PLM uses a modified sheath-limited regime which is not suited for detached divertors and (iv) the fact that the $B \times \nabla B$ drift direction is upwards, which leads to $E \times B$ drifts in the divertor that might affect the shape of the heat flux profile [67]. Note that for all the other shots in this study, $B \times \nabla B$ direction is towards the lower divertor.

By using a two-component input to the PLM, shown in figure 13 (right, brown dashed line), the far-SOL plateau and the peak value in the near-SOL can be matched, but not the shape of the profile. In this case, the ratio of the radial integral $\int q_{\perp,\text{FAR}-\text{SOL}} dr / \int q_{\perp,\text{NEAR}-\text{SOL}} dr$ is ~1, and ΔW_{ELM} input to the PLM is split among the slow and fast run accordingly i.e. 7.5 kJ each.

5.4. PLM simulations of type-I ELMs to an attached secondary divertor

Finally, the PLM model is benchmarked with IRTV data of attached type-I ELMs at the secondary outer divertor in unbalanced QDN (or 'weak' USN) configurations. Details on the design of this experiment can be found in [68]. In short, shots have ~identical plasma parameters but dR$_{\text{sep}}$ (i.e. the distance between primary and secondary separatrix measured at the OMP) is varied from +5.5 mm to +15 mm, as shown in figure 14(*a*). Figure 14(*b*) shows the magnetic configuration of a representative shot, with the IRTV view (secondary outer divertor) and the location of the secondary XPT. For these discharges, IRTV measurements are integrated over 200 μs (note that previous IRTV data presented in this paper have integration time of 80 μs), which, combined with the uncertainty in dRsep at DIII-D (~2–3 mm) causes the profiles to have an irregular shape in the vicinity of the separatrix.

In the simulations, filaments initial density and temperature are set to $T_e = 350$ eV and $n_e = 3 \times 10^{19}$ m^{-3} as measured at the top of the pedestal while the number of filaments, provided by ELITE runs, is set to 6 and $\Delta W_{\text{ELM}} = 70$ kJ. For this experiment, FRP measurements in the near-SOL are not available so we input the same radial velocity profile obtained with
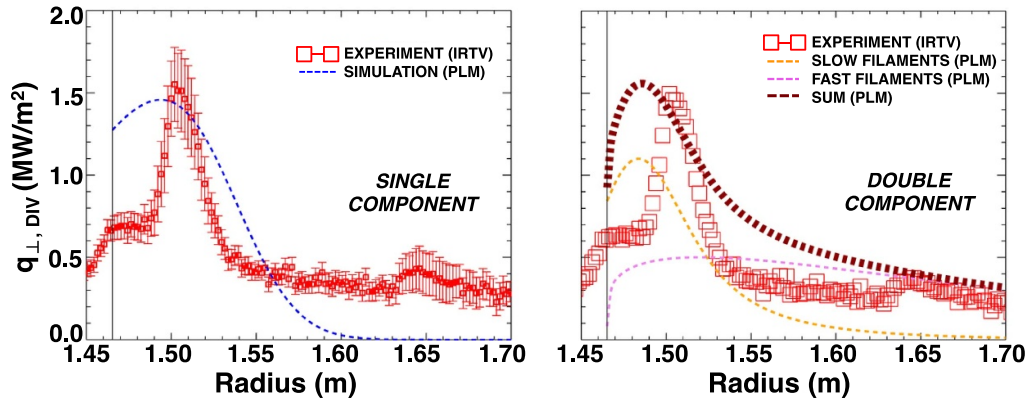
Figure 13. (Left) IRTV-PLM comparison for type-II ELM in detached divertor. The profiles shapes differ significantly in both near- and far-SOL but the peak heat flux is reproduced (right) IRTV-PLM comparison with the two-components approach. Note that error bars are shown only in the left plot.
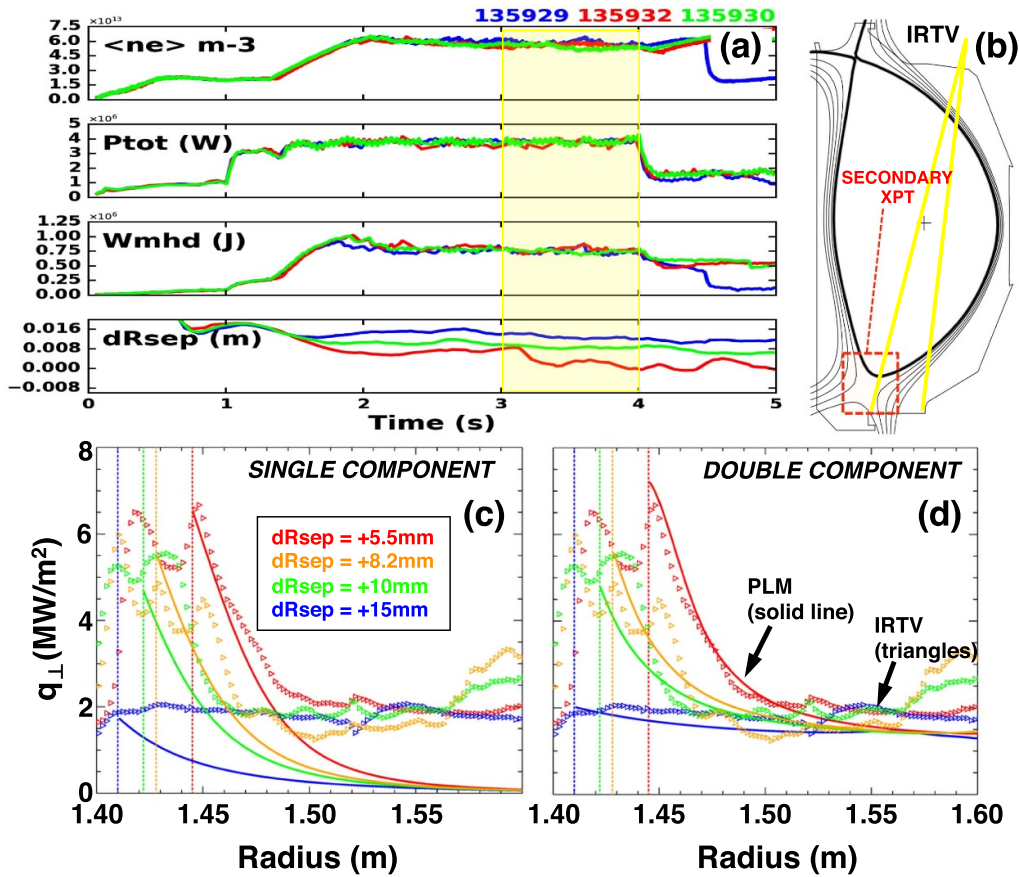

Figure 14. (*a*) Time traces of line-averaged density, total plasma power, plasma stored energy and dRsep. (*b*) EFIT reconstruction of one of the shots (#135932) with highlighted IRTV view and the secondary X-point. (*c*) IRTV-PLM comparison with single radial velocity component; heat flux peaks match within ∼20% but the plateau is not reproduced. (*d*) IRTV-PLM comparison with modified inputs employing a two component radial velocity showing significant improvement in the match to experimental data.

the sensitivity study for the attached type-I ELM case presented in section 5.1 (velocity at the separatrix of 0.191 km s^{-1} obtained with reflectometry and with decay length in the SOL $\lambda_v = 0.3$ m).

The comparison between the experimental data and single PLM runs, in figure 14(*c*), shows significant discrepancy between the profiles and the model does not reproduce the

plateau; however, the PLM peak heat flux decreases with increasing dRsep, with values that are within ∼20% of the experimental ones.

Simulations with two PLM runs for slow and fast filaments have been carried out in this scenarios, and the ELM energy sharing between the slow and fast component has been obtained by the ratio of the radially integrated near- and

far-SOL heat flux profile, as described in section 5.2, and found to be 37% and 63% for the fast and slow component, respectively. The radial velocities for the fast component are the same used in the attached LSN case i.e. 2.5 km s^{-1}. Results (figure 14(*d*)) reproduce the plateau and the radial integral of the simulated profiles, calculated outside the separatrix, is above 80% of the measured ones.

6. Discussion

ELM bursts are measured in the far-SOL region of the divertor and at several cm from the separatrix at the OMP, leading to a plateau that extends to the first wall in the time-averaged ELM heat flux profiles. In the case of attached divertor and type-I ELMs, these bursts are characterized by instantaneous peak heat fluxes comparable, or higher, to that in the vicinity of the strike point. Such ELM plasma transport to the far-SOL occurs for both type-I and small type-II ELMs, posing a concern for any future machine if those parts of the internal wall are not designed to withstand significant flux (note that the first and upper wall in ITER will have a power handling capability of ~1/3 of that at the main divertor [7]).

Plasma operations in ITER and other machines will likely be carried out in detached or partially detached divertor conditions, which, as shown by the experimental results presented in this work, provide a beneficial role in 'buffering' these far-SOL bursts before they reach the divertor target. This is observed in both type-I and small ELMing scenarios, the latter likely being the only acceptable ELMs in future devices.

ELM filaments are found to travel faster in detached conditions, where collisionality in the divertor increases, which is in line with the theory of filamentary plasma transport in the SOL. The ratio of the radially integrated near-SOL and far-SOL divertor heat flux in the case of type-II ELMs in a detached divertor is ~1, which is significantly lower than that for attached type-I ELMs i.e. ~1.8. The implications of this are that (i) faster radial transport of filaments in detached divertor leads to power being deposited over a wider surface compared to attached divertor but (ii) larger power loads to the first wall are to be expected when operating in such regime.

The results obtained by modeling the ELM filaments evolution with a two-component approach with the PLM support a concept where filaments undergo fragmentation, producing structures that vary in size and radial velocity, a part of which can reach the far-SOL and the first wall. This approach is justified by measurements and reproduces the experimental heat flux profiles, and should be further tested in other machines with different ELM size and divertor regimes.

7. Conclusions

The results presented in this paper can be summarized as follows:

- The conditionally-averaged heat flux profiles for type-I and type-II ELMs show a peak in the near SOL, which accounts

for 60%–70% of the total deposited energy to the target, and a plateau in the far-SOL accounting for the remaining ~30%–40%.
- The plateau extends >20 cm in the SOL along the divertor ($\Psi_n \sim 1.2$), which corresponds to R–$R_{\rm SEP,MID} \sim 8$ cm, implying significant flux to the first wall in future devices if the LCFS-first wall gap at the midplane is not sufficiently large.
- ELM heat flux bursts in the far-SOL are measured with IRTV and fast camera; however, IRTV measurements do not show the bursts in partially detached and detached divertors, suggesting dissipative mechanisms within the far-SOL divertor region.
- ELMs move radially faster in the near-separatrix in detached scenarios, consistent with high collisionality in the divertor, in line with the theory of filamentary plasma transport in the SOL [54].
- Within each ELM, discrete filamentary structures are observed and vary in radial velocity intermittently from ~0.2 to ~2.5 km s^{-1}.
- For the first time, the PLM model is tested with experimentally determined inputs such as the ELM radial velocity, $T_{\rm e}$ and $n_{\rm e}$ at the pedestal, ELM energy and filaments' size.
- The experimental ELM heat flux peak can be matched within ~20% with the PLM for attached, high-recycling and partially detached conditions. However, the model does not reproduce the plateau in the far SOL.
- The full ELM heat flux profiles can be reproduced by the model, within ~80%, by combining two separate PLM runs, one with slow and another with fast filaments.
- The PLM does not reproduce the heat flux profile for type-II ELMs in detached divertor conditions. PLM simulations with a two-component approach reproduce the peak heat flux and the plateau, but not the full divertor profile.

Further dedicated studies with non-linear codes e.g. BOUT++ [69] and JOREK [70] are needed to address the ELM filaments transport to the divertor far-SOL that causes heat flux bursts and the plateau in the time-averaged ELM profiles.

Further experiments on the interaction between ELM filaments radial velocity and divertor conditions are desirable, given its effect on the ELM heat flux footprint at the divertor and first wall power deposition.

Disclaimer

This report was prepared as an account of work sponsored by an agency of the United States Government. Neither the United States Government *nor* any agency thereof, nor any of their employees, makes any warranty, express or implied, or assumes any legal liability or responsibility for the accuracy, completeness, or usefulness of any information, apparatus, product, or process disclosed, or represents that its use would not infringe privately owned rights. Reference herein to any specific commercial product, process, or service by trade name, trademark, manufacturer, or otherwise does not necessarily constitute or imply its endorsement, recommendation, or favoring by the United States Government or any agency thereof. The views and opinions of authors expressed herein do not necessarily state or reflect those of the United States Government or any agency thereof.

ORCID iDs

R. Perillo ⬤ https://orcid.org/0000-0001-6696-5970
C.J. Lasnier ⬤ https://orcid.org/0000-0002-7109-2278
R.A. Pitts ⬤ https://orcid.org/0000-0001-9455-2698
J.D. Coburn ⬤ https://orcid.org/0000-0001-5618-0483
C. Marini ⬤ https://orcid.org/0000-0003-4819-7765
D.L. Rudakov ⬤ https://orcid.org/0000-0002-5266-4269

References

[1] Zohm E. 1996 *Plasma Phys. Control. Fusion* **38** 105
[2] Loarte A. *et al* 2003 *Plasma Phys. Control. Fusion* **45** 1549
[3] Kirk A., Wilson H.R., Counsell G.F., Akers R., Arends E., Cowley S.C., Dowling J., Lloyd B., Price M. and Walsh M. 2004 *Phys. Rev. Lett.* **92** 245002
[4] Moulton D., Ghendrih P., Fundamenski W., Manfredi G. and Tskhakaya D. 2013 *Plasma Phys. Control. Fusion* **55** 085003
[5] Leonard A.W. 2014 *Phys. Plasmas* **21** 090501
[6] Eich T., Sieglin B., Thornton A.J., Faitsch M., Kirk A., Herrmann A. and Suttrop W. 2017 *Nucl. Mater. Energy* **12** 84–90
[7] Pitts R.A. *et al* 2019 *Nucl. Mater. Energy* **20** 100696
[8] Snyder P.B., Wilson H.R., Ferron J.R., Lao L.L., Leonard A.W., Mossessian D., Murakami M., Osborne T.H., Turnbull A.D. and Xu X.Q. 2004 *Nucl. Fusion* **44** 320–8
[9] Creely A.J. *et al* 2020 *J. Plasma Phys.* **86** 865860502
[10] Leonard A.W. 2018 *Plasma Phys. Control. Fusion* **60** 044001
[11] Kukushkin A.S., Pacher H.D. and Pitts R.A. 2015 *J. Nucl. Mater.* **463** 586–90
[12] Evans T.E. *et al* 2008 *Nucl. Fusion* **48** 024002
[13] Fundamenski W., Pitts R.A. and J.E. Contributors 2006 *Plasma Phys. Control. Fusion* **48** 109
[14] Fundamenski W. and Pitts R.A. 2007 *J. Nucl. Mater.* **363–365** 319–24
[15] Pitts R.A., Fundamenski W., Erents S.K., Andrew Y., Loarte A., Silva C. and J.E. Contributors 2006 *Nucl. Fusion* **46** 82–98
[16] Kočan M., Pitts R.A., Lisgo S.W., Loarte A., Gunn J.P. and Fuchs V. 2015 *J. Nucl. Mater.* **463** 709–13
[17] Anand H., Pitts R.A., De Vries P.C., Snipes J.A., Kos L., Gribov Y., Zabeo L., Nunes I. and Brank M. 2020 *Nucl. Fusion* **60** 036011
[18] Brank M., Pitts R.A., Simič G., Lamalle P., Kocan M., Köchl F., Gribov Y., Polli V. and Kos L. 2021 *Nucl. Mater. Energy* **27** 101021
[19] Lasnier C.J., Hill D.N., Petrie T.W., Leonard A.W., Evans T.E. and Maingi R. 1998 *Nucl. Fusion* **38** 1225
[20] Herrmann A., Junker W., Gunther K., Bosch S., Kaufmann M., Neuhauser J., Pautasso G., Richter T. and Schneider R. 1995 *Plasma Phys. Control. Fusion* **37** 17
[21] Boedo J.A., Gray D., Chousal L., Conn R., Hiller B. and Finken K.H. 1998 *Rev. Sci. Inst.* **69** 2663
[22] Boedo J.A. *et al* 2001 *Phys. Plasmas* **8** 4826
[23] Marini C., Boedo J.A., Hollmann E.M., Chousal L., Mills J., Popović Z. and Bykov I. 2023 *Rev. Sci. Inst.* **94** 053509 accepted
[24] Zeng L., Peebles W.A., Doyle E.J., Rhodes T.L., Crocker N., Nguyen X., Wannberg C.W. and Wang G. 2014 *Rev. Sci. Inst.* **85** 11D843
[25] Eldon D. *et al* 2012 *Rev. Sci. Inst.* **83** 10E343
[26] Petrie T.W., Watkins J.G., Lao L.L. and Snyder P.B. 2003 *Nucl. Fusion* **43** 910–3
[27] Sauter O., Angioni C. and Lin-Liu Y.R. 1999 *Phys. Plasmas* **6** S1070
[28] Wilson H.R., Cowley S.C., Kirk A. and Snyder P.B. 2006 *Plasma Phys. Control. Fusion* **48** A71
[29] Leonard A.W. *et al* 2003 *J. Nucl. Mater.* **313–316** 768–76
[30] Stangeby P.C. 2018 *Plasma Phys. Control. Fusion* **60** 044022
[31] Krasheninnikov S.I., Kukushkin A.S. and Pshenov A.A. 2016 *Phys. Plasmas* **23** 055602
[32] Loarte A. *et al* 1998 *Nucl. Fusion* **38** 331
[33] Boedo J.A. *et al* 2005 *Phys. Plasmas* **12** 072516
[34] Huijsmans G.T.A. and Loarte A. 2013 *Nucl. Fusion* **53** 123023
[35] Herrmann A. *et al* 2007 *J. Nucl. Mater.* **363–365** 528–33
[36] Haskey S.R. *et al* 2018 *Plasma Phys. Control. Fusion* **60** 105001
[37] Pitts R.A., Chavan R., Davies S.J., Erents S.K., Kaveney G., Matthews G.F., Neill G., Vince J.E. and Duran I. 2003 *Rev. Sci. Inst.* **74** 4644
[38] Lao L.L., St. John H., Stambaugh R.D., Kellman A.G. and Pfeiffer W. 1985 *Nucl. Fusion* **25** 1611
[39] Kos L., Pitts R.A., Simič G., Brank M., Anand H. and Arter W. 2019 *Fusion Eng. Des.* **146** 1796–800
[40] Snyder P.B., Wilson H.R., Ferron J.R., Lao L.L., Leonard A.W., Osborne T.H., Turnbull A.D., Mossessian D., Murakami M. and Xu X.Q. 2002 *Phys. Plasmas* **9** 2037
[41] Perillo R., Boedo J.A., Lasnier C.J., Bykov I., Marini C. and Watkins J.G. 2022 *Phys. Plasmas* **29** 052506
[42] Lotte P., Aumeunier M.H., Devynck P., Fenzi C., Martin V. and Travère J.M. 2010 *Rev. Sci. Instrum.* **81** 10E120
[43] Moyer R.A. *et al* 2018 *Rev. Sci. Instrum.* **89** 10E106
[44] Eich T. *et al* 2005 *Plasma Phys. Control. Fusion* **47** 815
[45] Devaux S., Eich T., Arnoux G., Fundamenski W. and Thomsen H. 2011 *J. Nucl. Mater.* **415** S865–8
[46] Solano E.R. *et al* 2005 *J. Nucl. Mater.* **337–339** 747–50
[47] Solano E.R. *et al* 2008 *Nucl. Fusion* **48** 065005
[48] Sang C.F., Stangeby P.C., Guo H.Y., Leonard A.W., Covele B., Lao L.L., Moser A.L. and Thomas D.M. 2017 *Plasma Phys. Control. Fusion* **59** 025009
[49] Field A.R. *et al* 2017 *Plasma Phys. Control. Fusion* **59** 095003
[50] Bae M.-K., Pitts R.A., Bak J.G., Hong S.-H., Kim H.S., Lee H.H., Kang I.J. and Chung K.-S. 2017 *Nucl. Mater. Energy* **12** 1259–64
[51] Schmid A., Herrmann A. and Müller H.W. 2008 *Plasma Phys. Control. Fusion* **50** 045007
[52] Lampert M., Diallo A., Myra J.R. and Zweben S.J. 2021 *Phys. Plasmas* **28** 022304

[53] Kirk A. *et al* 2006 *Plasma Phys. Control. Fusion* **48** B433

[54] Krasheninnikov S.I. 2001 *Phys. Lett.* A **283** 368–70

[55] Tsui C.K. *et al* 2018 *Phys. Plasmas* **25** 072506

[56] D'Ippolito D.A. and Myra J.R. 2006 *Phys. Plasmas* **13** 062503

[57] Myra J.R., Russell D.A. and D'Ippolito D.A. 2008 *Phys. Plasmas* **15** 032304

[58] Theiler C., Furno I., Fasoli A., Ricci P., Labit B. and Iraji D. 2010 *Phys. Plasmas* **18** 055901

[59] He X.X., Xia T.Y., Wang Z.H., Tang T.F., Xu X.Q., Gao J.M., Huang Y.Q., Wu Y.B., Yang Z.C. and Liu Y. 2021 *AIP Adv.* **11** 035334

[60] Kim M., Park H.K., Lee J., Yun G.S., Xu X.Q. and Bécoulet M. 2019 *Phys. Plasmas* **26** 052502

[61] Xu X.Q., Dudson B.D., Snyder P.B., Umansky M.V., Wilson H.R. and Casper T. 2011 *Nucl. Fusion* **51** 103040

[62] Ionita C. *et al* 2013 *Nucl. Fusion* **53** 043021

[63] Gonçalves B., Hidalgo C., Pedrosa M.A., Silva C., Balb N R., Erents K., Hron M., Loarte A. and Matthews G. 2003 *Plasma Phys. Control. Fusion* **45** 1627

[64] Müller H.W. *et al* 2011 *Nucl. Fusion* **51** 073023

[65] Garcia O.E., Bian N.H., Naulin V., Nielsen A.H. and Rasmussen J.J. 2006 *Phys. Scr.* **T122** 104–24

[66] Akkermans G.R.A., Classen I.G.J., Perillo R., van der Meiden H.J., Federici F. and Brezinsek S. 2020 *Phys. Plasmas* **27** 102509

[67] Jaervinen A.E. *et al* 2019 *Nucl. Mater. Energy* **19** 230–8

[68] Perillo R., Boedo J.A., Lasnier C.J., Rudakov D.L., Osborne T. and Watkins J.G. 2021 *Nucl. Fusion* **61** 086024

[69] Omotani J.T., Dudson B.D., Havlíčková E. and Umansky M. 2015 *J. Nucl. Mater.* **463** 769–72

[70] Huysmans G.T.A. and Czarny O. 2007 *Nucl. Fusion* **47** 659–66